Volume 14 | Number 7 | July 2015 | Pages 1215–1368

Photochemical & Photobiological Sciences

An international journal

www.rsc.org/pps

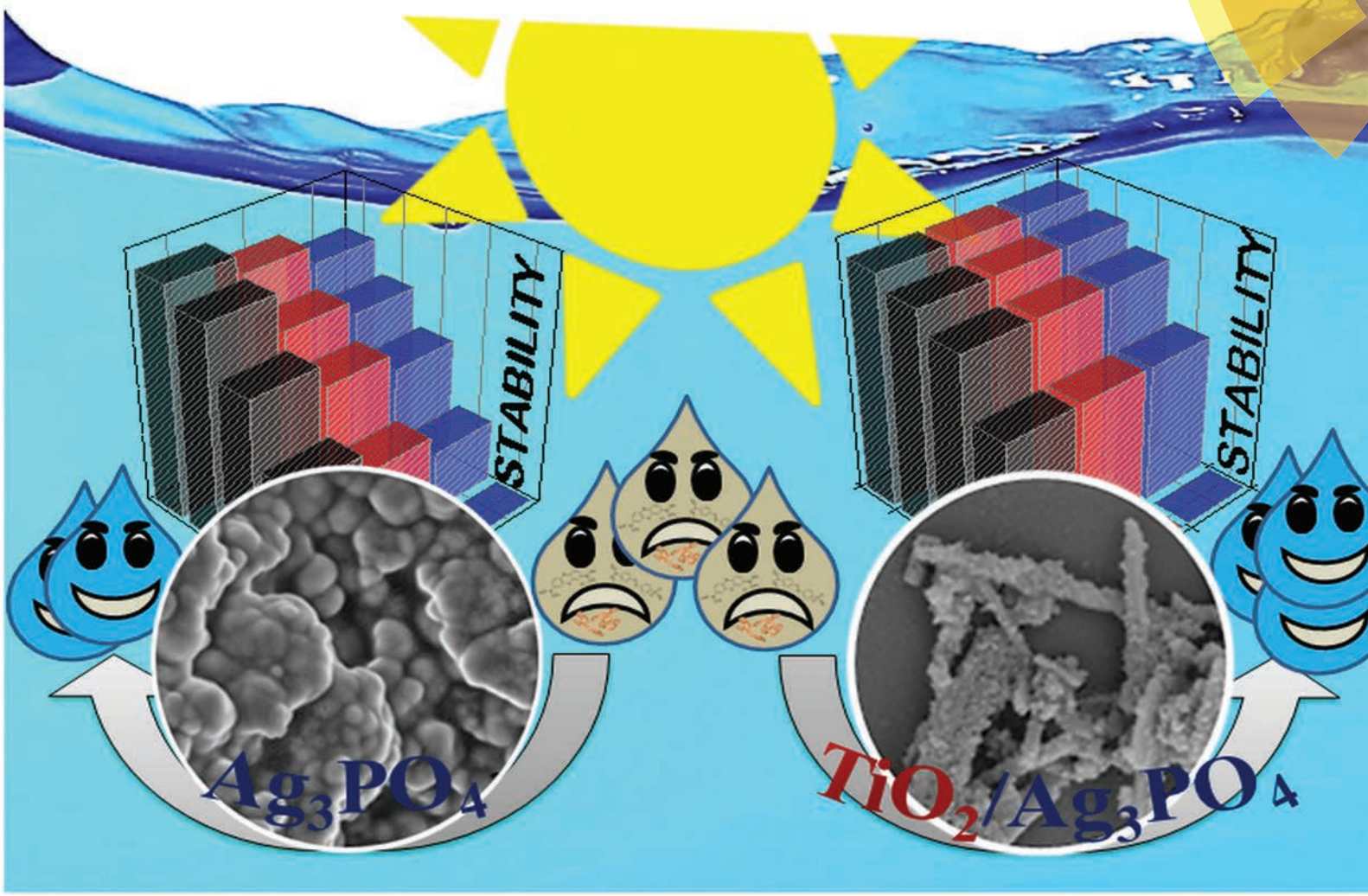

ISSN 1474-905X

ROYAL SOCIETY OF CHEMISTRY

EPA ESP KOREAN SOCIETY OF PHOTOSCIENCE APSP

Photochemical & Photobiological Sciences

PAPER

View Article Online
View Journal | View Issue

Cite this: *Photochem. Photobiol. Sci.*, 2015, **14**, 1227

Enhanced sunlight photocatalytic activity of Ag_3PO_4 decorated novel combustion synthesis derived TiO_2 nanobelts for dye and bacterial degradation

Neerugatti KrishnaRao Eswar,[a] Praveen Chandrashekarapura Ramamurthy[a,b] and Giridhar Madras*[c]

Received 4th March 2015,
Accepted 20th May 2015

DOI: 10.1039/c5pp00092k

www.rsc.org/pps

This study demonstrates the synthesis of TiO_2 nanobelts using solution combustion derived TiO_2 with enhanced photocatalytic activity for dye degradation and bacterial inactivation. Hydrothermal treatment of combustion synthesized TiO_2 resulted in unique partially etched TiO_2 nanobelts and Ag_3PO_4 was decorated using the co-precipitation method. The catalyst particles were characterized using X-ray diffraction analysis, BET surface area analysis, diffuse reflectance and electron microscopy. The photocatalytic properties of the composites of Ag_3PO_4 with pristine combustion synthesized TiO_2 and commercial TiO_2 under sunlight were compared. Therefore the studies conducted proved that the novel Ag_3PO_4/unique combustion synthesis derived TiO_2 nanobelt composites exhibited extended light absorption, better charge transfer mechanism and higher generation of hydroxyl and hole radicals. These properties resulted in enhanced photodegradation of dyes and bacteria when compared to the commercial TiO_2 nanocomposite. These findings have important implications in designing new photocatalysts for water purification.

1. Introduction

As a result of radical urbanization, the quality of water has been compromised. Further, improper waste water treatment in industries dumping of wastes causes water pollution. Besides chemical contamination, bacterial infections pertaining to water contamination must also be considered seriously. Fecal bacteria such as *Escherichia*, fecal coliforms, *Staphylococcus, Pseudomonas*, and *Streptococcus* species in water cause various infections[1] and are a menace to public health.[2] The primary objective of any disinfection process in water treatment is the control of water-borne diseases through inactivation of pathogenic microorganisms in the water.[3]

Generation of reactive oxygen species to degrade the chemical contaminants and pathogens by an advanced oxidation process using nanoparticles is one of the solutions for water purification. Over the past few years, research on nanomaterials is increasing rapidly because of their valuable properties. There are several methods for the synthesis of nanomaterials and varying morphologies such as nanorods, spheres, discs, nanoflowers, platelets *etc.*[4,5] have been obtained and used for different applications like photocatalysis, electrocatalysis, supercapacitors *etc.*[6,7]

Metal oxides such as ZnO, TiO_2 *etc.* and metals like Ag and Au have been used for various catalytic applications.[8,9] Among various routes such as sol–gel, hydrothermal, solvothermal, aerosol, inert gas condensation, combustion synthesis of nanomaterials is considered to be quick and efficient. Combustion synthesized TiO_2 has proved to be an efficient catalyst compared to its commercial counterpart.[10,11] However, many studies have attempted to increase the photoactivity of TiO_2, since its efficiency depends on parameters such as particle size, crystallinity, pore size[12] *etc.* Efforts have been made to increase the photoactivity by doping it with various transition elements.[13]

Silver and silver based compounds such as AgBr, AgI, Ag_3PO_4, have been used for photocatalytic and antibacterial applications.[14–16] Silver is being used as an effective antimicrobial agent because it exhibits strong cytotoxic activity against a broad range of microbial organisms.[17] Recently, in addition to pristine silver, silver based photocatalysts are used widely for photocatalytic applications. AgBr on $AgVO_3$ nanobelts has shown efficient plasmonic photocatalytic activity against Rhodamine-B with good stability.[16] Surfactant assisted highly-crystalline AgI nanoplates showed better photocatalytic activity under visible light.[14] Ag_3PO_4 and Ag/Ag_3PO_4 showed better

[a]*Centre for Nanoscience and Engineering, Indian Institute of Science, Bangalore-560012, India*
[b]*Department of Materials Engineering, Indian Institute of Science, Bangalore-560012, India*
[c]*Department of Chemical Engineering, Indian Institute of Science, Bangalore-560012, India. E-mail: giridhar@chemeng.iisc.ernet.in; Fax: +91 80 23600683; Tel: +91 80 22932321*

absorption of visible light and exhibit excellent antibacterial activity.[18] Recent studies on the activity of the AgBr composite with iron oxide have reported enhanced photocatalytic activity under visible light.[19,20] Similarly the Ag_3PO_4 composite with TiO_2·Fe_2O_3 and GO has shown better and synergistic photocatalytic activity compared to its pristine composition, also by facilitating magnetic separation of the photocatalyst.[21–24]

In this study, TiO_2 (CST) was prepared by the solution combustion method using ascorbic acid as a reducer. Recent reports have shown that as the nature of the TiO_2 precursors varies, the attributes of the nanobelts derived from them change significantly.[25] The TiO_2 nanobelts (CSTNB) were synthesized using combustion synthesized TiO_2 as a novel precursor. Ag_3PO_4 has been impregnated on these TiO_2 nanobelts by the simple co-precipitation technique. This is the first study to report impregnation of Ag_3PO_4 on TiO_2 nanobelts prepared using combustion synthesized TiO_2 as a precursor for photocatalysis under natural sunlight. The photocatalytic degradation of organic pollutants and antibacterial activity of Ag_3PO_4 impregnated combustion synthesized TiO_2 and TiO_2 nanobelt compounds have been compared with commercial TiO_2 (Degussa P-25).

2. Experimental

2.1 Materials

Titanium iso-propoxide (>97% purity) was purchased from Sigma-Aldrich. L-Ascorbic acid-LR, silver nitrate, di-sodium hydrogen phosphate and methylene blue, methyl orange, neutral red dyes were purchased from SD Fine Chemicals Ltd (India). Sodium hydroxide, sulphuric acid (98%), hydrochloric acid (35%) and nitric acid (69%) were purchased from Merck (India). The Neubauer-chamber was purchased from Pristine Scientific Ltd (India). Luria nutrient broth was purchased from Hi Media (India). Double distilled Millipore water was used for all the experiments.

2.2 Catalyst preparation

2.2.1 Synthesis of TiO_2 using the solution combustion method. TiO_2 nanoparticles were prepared using the solution combustion method[10] with ascorbic acid as a reducer and titanyl nitrate as an oxidizer. A typical synthesis of titanyl nitrate involves mixing titanium iso-propoxide in ice-cold water to obtain a white precipitate. To the above precipitate, 1 : 2 nitric acid (by volume) was added to obtain a transparent solution of titanyl nitrate. An equimolar oxidizer to fuel ratio was maintained by adding titanyl nitrate with a stoichiometric amount of L-ascorbic acid. The combustion reaction is;

$$2TiO(NO_3)_2 + C_6H_8O_6 \xrightarrow{350\,^{\circ}C} 2TiO_2 + 6CO_2 + 4H_2O + 2N_2 \quad (1)$$

The reaction mixture was kept in a preheated furnace at 350 °C for 15 min and a smoldering combustion reaction was observed. The combustion product was ground finely to obtain a pale yellow colored powder.

2.2.2 Synthesis of TiO_2 nanobelts from combustion synthesized TiO_2. TiO_2 nanobelts (CSTNB) were prepared from combustion synthesized TiO_2.[26] 20 ml of 10 M sodium hydroxide was mixed with 0.1 g of combustion synthesized TiO_2 and stirred vigorously. Later the mixture was transferred into Teflon coated steel autoclave and kept inside the furnace at 180 °C for 48 h. The nature of nanobelt remains the same by varying the temperature of the hydrothermal reaction from 180 °C to 240 °C.[27,28] Hence, the optimum temperature is considered as 180 °C and 48 h. Similarly, after hydrothermal treatment of TiO_2 with NaOH, $Na_2Ti_3O_7$ is formed. The obtained powder was washed with de-ionized water several times to remove impurities and then dispersed in 0.1 M HCl. Treating this product with HCl involves ion exchange to become $H_2Ti_3O_7$. In order to remove the impurities, the product formed was thoroughly washed with de-ionized water until the pH of the washed solution became 7. Later $H_2Ti_3O_7$ belts were dispersed in 40 ml of 0.02 M sulphuric acid and transferred to a Teflon coated steel autoclave. The autoclave was maintained at 100 °C for 12 h to obtain acid etched $H_2Ti_3O_7$ belts. However, the increase in concentration or reaction time during acid corrosion of combustion synthesis derived TiO_2 nanobelts changes the structure of belts by disintegrating them into fine nanoparticles. Hence, 0.02 M of H_2SO_4 and 12 h reaction at 100 °C were considered as optimal. The resulting product was centrifuged at 5000 rpm for 10 min and washed several times with de-ionized water, and later dried at 70 °C for 10 h. The dried powder was annealed at 600 °C for 2 h to obtain white colored acid etched TiO_2 nanobelts (CSTNB).

2.2.3 Synthesis of Ag_3PO_4, Ag_3PO_4/CST and Ag_3PO_4/CSTNB. A simple co-precipitation technique was used to prepare Ag_3PO_4/CST and Ag_3PO_4/CSTNB heterostructures. Initially, 0.2 g acid-etched TiO_2 nanobelts (CSTNB) were dispersed in 100 ml of de-ionized water in a separate round bottom flask. The mixture was ultrasonicated for 15 min. A stoichiometric amount of silver nitrate and di-sodium hydrogen phosphate solution was prepared separately using de-ionized water. Silver nitrate solution (1 : 10 of Ag_3PO_4 : TiO_2) was added dropwise to the TiO_2 nanobelt dispersed mixture while continuing with vigorous stirring at 60 °C. The pH of the mixture was kept at 5 using 0.1 M nitric acid.

For comparison, the same process was carried out for the preparation of Ag_3PO_4/CST and Ag_3PO_4/P-25 using combustion synthesized TiO_2 and commercial Degussa P-25 instead of TiO_2 nanobelts. Di-sodium hydrogen phosphate solution was added slowly into the above mixture until the solution turned pale yellow indicating the formation of Ag_3PO_4 on CST and CSTNB. Pristine Ag_3PO_4 was prepared by the same procedure but without the addition of TiO_2 nanoparticles.

3. Characterization

X-ray diffraction spectra were obtained from a Rigaku diffractometer using Cu-Kα radiation with a scan rate of 1° min^{-1} in the scan range of 10°–80°. Scanning electron micrographs

were captured using ULTRA55 FESEM, Carl Zeiss. The samples were dispersed in absolute ethanol and sonicated for 10 min. These dispersed samples were drop-casted on silica wafers which were stuck to a carbon tape on a SEM aluminium stub. The prepared samples were kept under vacuum for 12 h; after that samples were gold sputtered using a Quaram sputtering machine to prevent the sample charging effect and SEM images were taken. Transmission electron micrographs were acquired with a Tecnai T20 operated at 180 kV. Samples for TEM analysis were prepared by dispersing it in isopropanol and subjected to ultrasonication. Later, the samples were drop casted on copper grid and kept under vacuum for 12 h. Diffuse reflectance spectra were obtained using a solid state UV-visible spectrophotometer (Perkin Elmer). Photoluminescence measurements were performed using a PL-spectrophotometer (Perkin Elmer). The absorbance measurements for photocatalysis experiments were measured using a UV-Visible spectrophotometer (Shimadzu-UV 1700). Samples were regenerated at 120 °C for 2 h prior to BET surface analysis using Nova-1000 Quantachrome. The data were obtained by using a Belsorb surface area analyzer (Smart instruments) with the help of liquid nitrogen (77 K) and water (300 K) atmospheres for both adsorption and desorption of N_2.

4. Photochemical reactor and photocatalysis

100 ml quartz reactors were used to perform photocatalytic experiments. Photocatalytic dye degradation and antibacterial degradation experiments were conducted under direct sunlight between 11:00 am and 2:00 pm, when the solar intensity fluctuations are less and the intensity was ~975 W m^{-2}. The reaction mixture was stirred vigorously using a magnetic stirrer and the samples were collected from the reactor at a specific time to measure absorbance. Experiments were performed in the dark to measure the adsorption of the dye over catalyst particles.

Photocatalysis was performed using a 20 ppm aqueous solution of methylene blue and a 30 ppm aqueous solution of methyl orange. The catalyst concentration was maintained at 1 g l^{-1} for all the experiments. The catalyst particles were initially suspended in the dye solution and kept in the dark for 1 h to achieve stable absorption–desorption equilibrium. Samples were collected from the reactor at regular intervals and centrifuged at 5000 rpm for 5 min to separate catalyst particles from the solution and absorbance was measured using a UV-visible spectrophotometer.

4.1. Antibacterial evaluation

The bacterial culture of wild type *Escherichia coli* strain was prepared using liquid nutrient broth. Glass ware, media, test tubes, Eppendorf tubes, micro tips *etc*. and all other accessories required for culture preparation and antibacterial evaluation were autoclaved and kept under UV light inside a laminar chamber. The bacterial culture was centrifuged at 5000 rpm for 10 minutes to separate bacterial cells as pellets. Later, the pellets were re-suspended in phosphate buffer saline solution in order to maintain the ionic concentration for the bacteria. Control experiments were conducted in the dark using 0.25 g l^{-1} catalyst and bacterial suspension alone without keeping the reactor under solar irradiation. Furthermore, the catalysts were added into a fresh bacterial suspension and kept under solar radiation. Sample mixtures of bacterial and catalyst suspensions were collected at regular intervals in order to measure antibacterial activity. Various methods such as broth dilution, turbidity assay, colony-counting, disk-diffusion, growth inhibition and minimum inhibitory concentration were used. In addition to these, Neubauer-chamber counting can be used for the quantitative or qualitative determination of anti-microbial activity.[29,30] 100 μl of serially diluted aliquots were mixed with 0.4% of a neutral red solution according to a 1 : 10 ratio. 20 μl of the above stained bacterial suspension was pipetted out on a Neubauer counting chamber. The viable bacterial cells were stained by neutral red because live cells incorporate the stain into lysosomes. Live bacterial cells were counted on respective squares under a microscope and averaged for calculating bacterial cell density.

5. Results and discussion

5.1. X-ray diffraction analysis

X-ray diffraction patterns of combustion synthesized TiO_2 and acid etched TiO_2 nanobelts are shown in Fig. 1(a) and (b). The synthesized product with ascorbic acid as the fuel for combustion has shown the possibility of formation of a rutile phase at 2θ values of 36.0° and 54.2° (JCPDS no: 00-001-1292) besides a predominant anatase phase. The anatase can be observed at a 2θ value of 25.4° (JCPDS no: 00-004-0477) with (101) as <*hkl*> parameters. It has been reported that combustion synthesis of TiO_2 using titanyl nitrate and ascorbic acid of 5 : 3 molar ratio between the oxidizer and the fuel resulted in a pure anatase phase.[31] However, if the stoichiometric ratio is 2 : 1, the rutile phase is formed which co-exists with anatase.

The X-ray diffraction pattern of nanobelts prepared out of combustion synthesized TiO_2 shows a huge peak that corresponds to the anatase phase (JCPDS no: 00-004-0477) and adjacent to it a small peak at 27.6° corresponding to the rutile phase (JCPDS no: 00-001-1292). The diffraction peaks for Ag_3PO_4 nanoparticles are denoted with filled dots (Fig. 1(c)) and at 33.4° a huge peak was observed which corresponds to (210) plane diffraction. Further peaks at 36.7°, 55.0°, 57.5°, and 61.9°, can be assigned to the diffractions from the (2 1 0), (3 1 0), (3 2 0), (3 2 1), and (4 0 0) planes of Ag_3PO_4 (JCPDS (00-006-0505)). This pattern was also manifested in the Ag_3PO_4/TiO_2 nano heterostructures (Fig. 1(d)). Therefore, successful impregnation of Ag_3PO_4 over acid etched TiO_2 nanobelts can be corroborated based on these observations.

5.2. Diffuse reflectance spectrophotometry

The UV-vis diffuse reflectance spectra of the Ag_3PO_4, acid etched TiO_2 nanobelts and Ag_3PO_4 coupled acid etched TiO_2 nanobelts were measured using a UV-Vis spectrophotometer

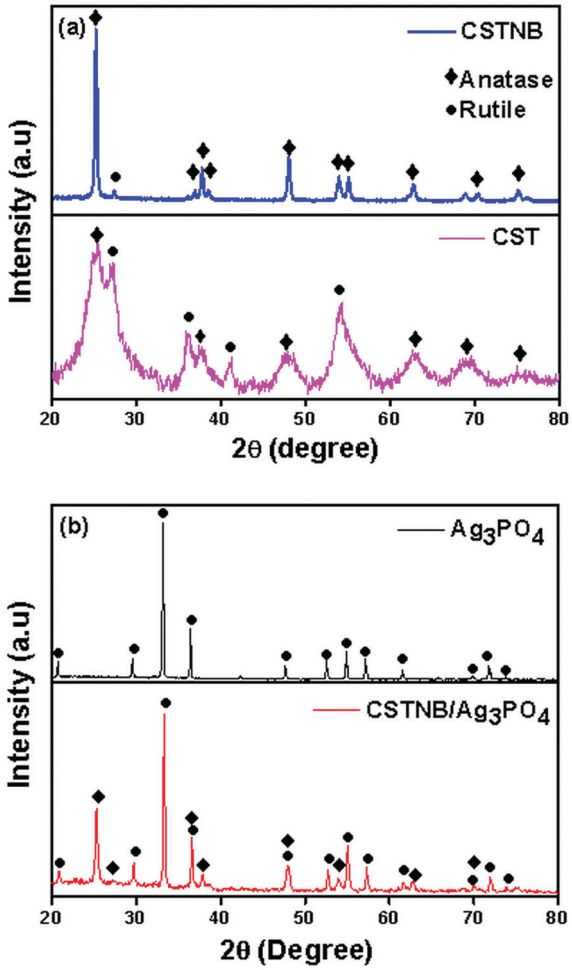

Fig. 1 (a) X-ray diffraction pattern of combustion synthesized TiO_2 and acid etched TiO_2 nanobelts and (b) X-ray diffraction pattern of Ag_3PO_4 and Ag_3PO_4 coupled with acid etched TiO_2 nanobelts.

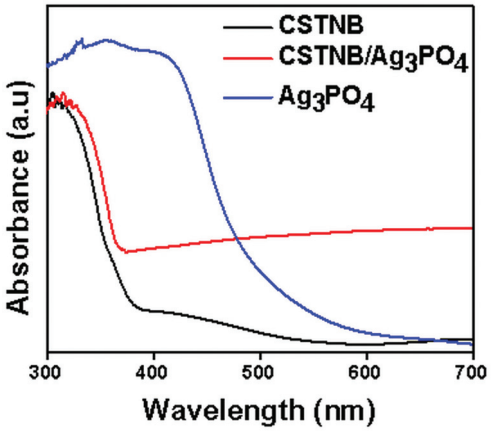

Fig. 2 Diffuse reflectance spectra of Ag_3PO_4, CSTNB and Ag_3PO_4/CSTNB.

(Perkin Elmer). The formation of Ag_3PO_4/TiO_2 has accounted for a remarkable increase in light absorption in the visible region compared to pristine TiO_2 nanobelts. As shown in Fig. 2, UV-vis diffuse reflectance spectroscopy measurements rendered that the acid-etched TiO_2 nanobelts exhibited a strong absorption at about 390 nm, which can correspond to the band gap of multi-phase titania having both anatase and rutile phases (3.0–3.2 eV).[32] Similarly, a strong absorption peak was recorded at around 550 nm which can be matched to Ag_3PO_4 nanoparticles whose in-direct band gap was calculated to be around 2.4 eV.[33] The absorption edge of the Ag_3PO_4 impregnated TiO_2 heterostructures was unaltered compared to the pristine acid etched TiO_2 nanobelts. However, there was a strong absorbance in the visible region between 400 and 700 nm. This can confirm that Ag_3PO_4 was successfully impregnated over the acid etched TiO_2 nanobelts.[33,34]

5.3. Microscopy analysis

The morphological features of acid etched TiO_2 nanobelts and Ag_3PO_4 impregnated TiO_2 nanobelts were studied using SEM and HRTEM micrographs. The SEM image of acid etched TiO_2 nanobelts before acid treatment is shown in Fig. 3(a). An acid corrosion treatment led to partial etching of nanobelts and subsequent formation of several TiO_2 islands on existing nanobelts and also on partially etched nanobelts, as shown in Fig. 3(b). The surface area of TiO_2 nanobelts was 35 m^2 g^{-1} and it increases to 75 m^2 g^{-1} after the acid etching process.[35] It can be suggested that the etched surfaces could serve as nucleating sites for Ag_3PO_4 nanoparticles, resulting in the formation of Ag_3PO_4/TiO_2 composites, as shown in (Fig. 3(c)). One can observe that the Ag_3PO_4 nanoparticles, with an approximate diameter between 10 and 20 nm, were deposited onto the acid-etched TiO_2 nanobelt surface, consistent with the TEM image shown in Fig. 3(e). Ag_3PO_4 nanoparticles were also prepared without the acid etched TiO_2 nanobelt support, following similar experimental conditions excluding the addition of TiO_2 nanobelts. Ag_3PO_4 nanoparticles were spherical in shape and mostly agglomerated with other particles, as shown in Fig. 3(d). The structural analysis of the Ag_3PO_4/TiO_2 heterostructures was done by HRTEM.

As shown in Fig. 3(f), the lattice of both Ag_3PO_4 and TiO_2 can be clearly distinguished. Ag_3PO_4 particles have a *d*-spacing of 0.56 nm, matching with the structure of Ag_3PO_4, whereas a *d*-spacing of 0.35 nm was observed for the TiO_2 nanobelts, which corresponds to anatase TiO_2. It can be clearly observed that the Ag_3PO_4 was impregnated firmly into the TiO_2 nanobelt substrate, which promotes a synergistic effect towards photocatalysis by promoting a wide optical absorption and also ensures structural stability of the composite.

5.4. X-ray photoelectron spectroscopy

XPS results of silver in Ag_3PO_4/CSTNB show the existence of Ag in two bands corresponding to 368.2 and 374.1 eV, respectively, ascribed to Ag $3d_{5/2}$ and Ag $3d_{3/2}$ (Fig. 4(a)). These bands correspond to the Ag^+ of Ag_3PO_4. The bands observed in Fig. 4(b) at 369.2 and 374.9 eV exhibit the binding energy of silver in the Ag^0 state. This proves that after exposing Ag_3PO_4 (either in

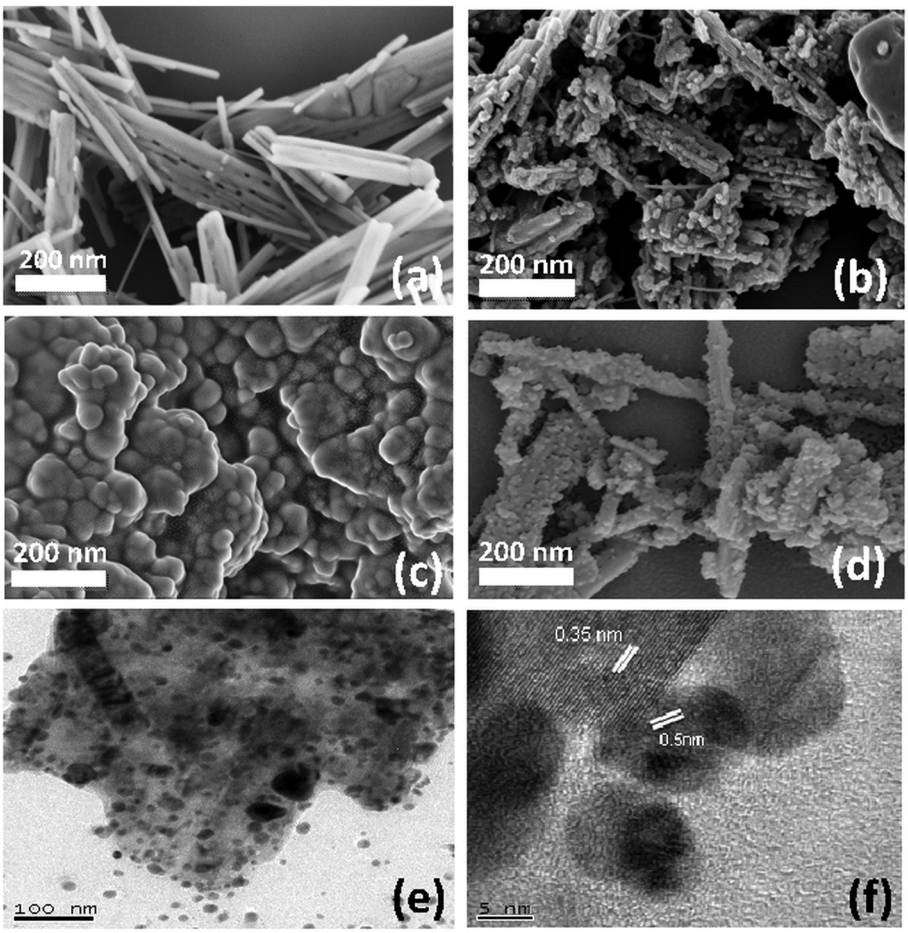

Fig. 3 Scanning electron microscopy images of (a) pristine nanobelts, (b) acid etched TiO2 nanobelts, (c) Ag_3PO_4, (d) Ag_3PO_4/acid etched TiO_2 nanobelt composite, bright field TEM image of (e) Ag_3PO_4/acid etched TiO_2 nanobelt composite and HRTEM image of (f) Ag_3PO_4/acid etched TiO_2 nanobelt composite.

pristine or composite form) to light, part of Ag^+ becomes Ag^0. In the case of just Ag_3PO_4, the Ag^0 formation is very high and hence stability is low. However, when Ag_3PO_4 is in the composite form, there will be a formation of the Ag/Ag_3PO_4/substrate[36] and hence a prolonged activity of Ag_3PO_4 is maintained.

5.5. Photoluminescence spectroscopy

The photoluminescence spectra of Ag_3PO_4 impregnated combustion synthesized TiO_2 and acid etched TiO_2 nanobelts are shown in Fig. 5. The presence of intrinsic states instead of surface states can be corroborated to the peak originating at 419 nm because of charge transfer transitions between the 2p orbitals of oxygen and the empty d orbital of the silver ion which could possibly lead to recombination during photoluminescence.[37] Recombination of self-trapped excitons in the PO_4 anionic complex could also be the reason for the emission peak at 419 nm. The peak at 533 nm which is approximately equal to the band gap of Ag_3PO_4 can be matched to the recombination of electrons at the conduction band and holes at valence band edges.[38,39] Surface deposited silver or Ag doped into the TiO_2 lattice can act as efficient traps for the photo-induced electrons that prevent recombination. However, the presence of excess Ag^0 could lead to reduction in the traps and increase in photoluminescence intensity as observed at 441 nm and 485 nm. The peak at 530 nm can also correspond to charge transfer between oxygen vacancies and Ti^{4+} including the peak at 460 nm which acts as a trap for charge.[40] In the case of Ag_3PO_4 impregnated with acid etched TiO_2 nanobelts the photoluminescence intensity decreased significantly which can be attributed due to an efficient charge transfer and charge separation mechanism.

5.6. Photocatalysis

5.6.1. Photocatalytic degradation of dyes. The photocatalytic performance of Ag_3PO_4/CST and Ag_3PO_4/CSTNB was assessed by the degradation of organic dye molecules under sunlight irradiation. Fig. 6(a) and (b) show the degradation of both cationic (methylene blue) and anionic (methyl orange) dyes. These catalysts were compared to the composite of Ag_3PO_4 with standard commercial grade TiO_2, Degussa P-25 (Ag_3PO_4/P-25). Photodegradation experiments were also conducted using pristine Ag_3PO_4. The blank experiments were

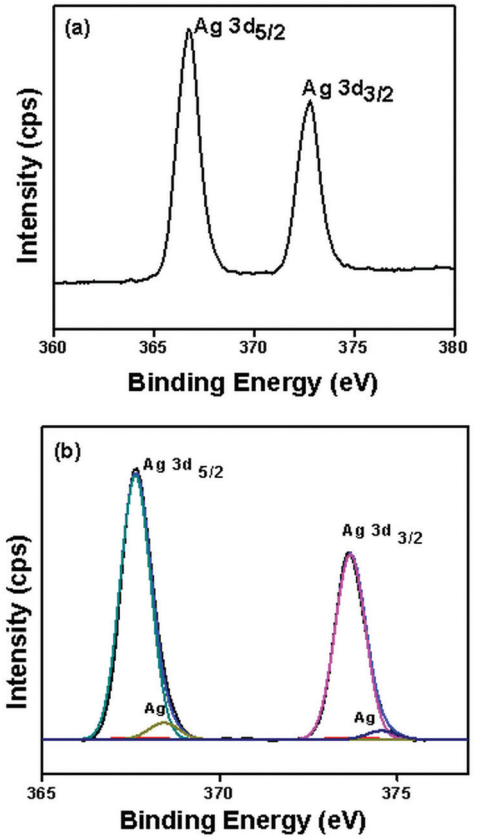

Fig. 4 XPS spectra of Ag in Ag_3PO_4/CSTNB (a) before the reaction (b) after the reaction.

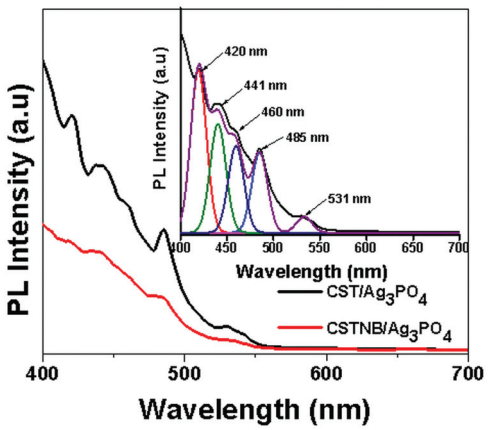

Fig. 5 Photoluminescence spectra of Ag_3PO_4/CST and Ag_3PO_4/CSTNB (inset peak positions).

conducted in the absence of sunlight, where the catalysts were experimented for adsorption. All the catalysts showed adsorption at around 15% of the initial dye concentration. Pristine Ag_3PO_4 showed negligible adsorption over both the dyes. The photocatalytic efficiency of Ag_3PO_4/CSTNB was significantly higher compared to other composites. Though the photocatalytic activity of Ag_3PO_4 was higher compared to the composites, the stability of Ag_3PO_4 reduced over subsequent runs.[34] Ag_3PO_4/TiO_2 nanobelts showed very high photocatalytic activity for all the dyes. This is due to efficient charge separation that could happen in the TiO_2 nanobelts and also potential charge transfer at the interface of acid etched TiO_2 nanobelts and Ag_3PO_4. Both the cationic and anionic dyes degraded 100% within 20 and 30 min, respectively, under solar irradiation with Ag_3PO_4/CSTNB. However, in the presence of Ag_3PO_4/CST and Ag_3PO_4/P-25, it took 30 and 40 min respectively for the dyes to degrade completely. The degradation was analyzed by plotting C/C_0 with time. $\ln(C/C_0) = kt$ is the first order kinetic equation that corresponds to the photocatalytic degradation, where C_0 is the initial concentration, C is the final concentration of the reactant at time t and k is the apparent rate constant. The slope of the linear plot of $\ln(C/C_0)$ *versus* time gives the apparent rate constant k. The apparent rate constants of all the catalysts are tabulated (Table 1). From the kinetic plot, as shown in Fig. 6(c) and (d), the rate constant obtained for Ag_3PO_4/CSTNB for both methylene blue and methyl orange degradation was very high compared to Ag_3PO_4/CST and Ag_3PO_4/P-25 indicating its superior photocatalytic activity. The efficient charge separation because of island–belt interactions, the majority of active phase exposure, and a wide range of optical absorption of light by the composite could be possible reasons for the enhanced photoactivity exhibited by Ag_3PO_4 coupled acid etched TiO_2 nanobelts.

5.6.2. Antimicrobial activity. The bacterial degradation experiments were performed under natural sunlight using Ag_3PO_4/P-25, Ag_3PO_4/CST, Ag_3PO_4/CSTNB and Ag_3PO_4. Photolysis experiments were performed without any catalyst particles in the bacterial suspension. Control experiments were also carried out using just the catalysts in the bacterial suspension but in the absence of sunlight as shown in Fig. 7(a). From Fig. 7(b), it is evident that Ag_3PO_4/CSTNB was efficient for the inactivation of the microorganisms compared to other composites. Pristine Ag_3PO_4 shows high antimicrobial activity against *E. coli*. Ag_3PO_4 can also slowly release Ag ions into the solution. Therefore, the composites have shown significant bacterial reduction compared to their TiO_2 counterpart in the composite. Upon exposure to sunlight, Ag_3PO_4 turned dark within a short period of time unlike the composites, indicating that part of Ag^+ was reduced to Ag^0. The reactive radical species generated by the catalyst was responsible for killing the bacteria. The generated radicals would break the polyunsaturated phospholipid structures that are present in *E. coli*, which ruptures the cell membrane leading to bacterial degradation[41,42] and also damages the nucleic matter of bacteria.[43,44] Therefore, Ag_3PO_4 coupled with acid-etched TiO_2 nanobelt structures exhibits superior antibacterial activity by generating more hydroxyl radicals combined with the synergistic effect of Ag.[45] In the dark experiments, the antibacterial activity of Ag_3PO_4 and composites is due to the release of Ag^+ ions. Silver ions and silver nanoparticles are efficient bactericidal agents.[46] Therefore, upon irradiating with sunlight, Ag_3PO_4 acts as an efficient semiconductor, where charge

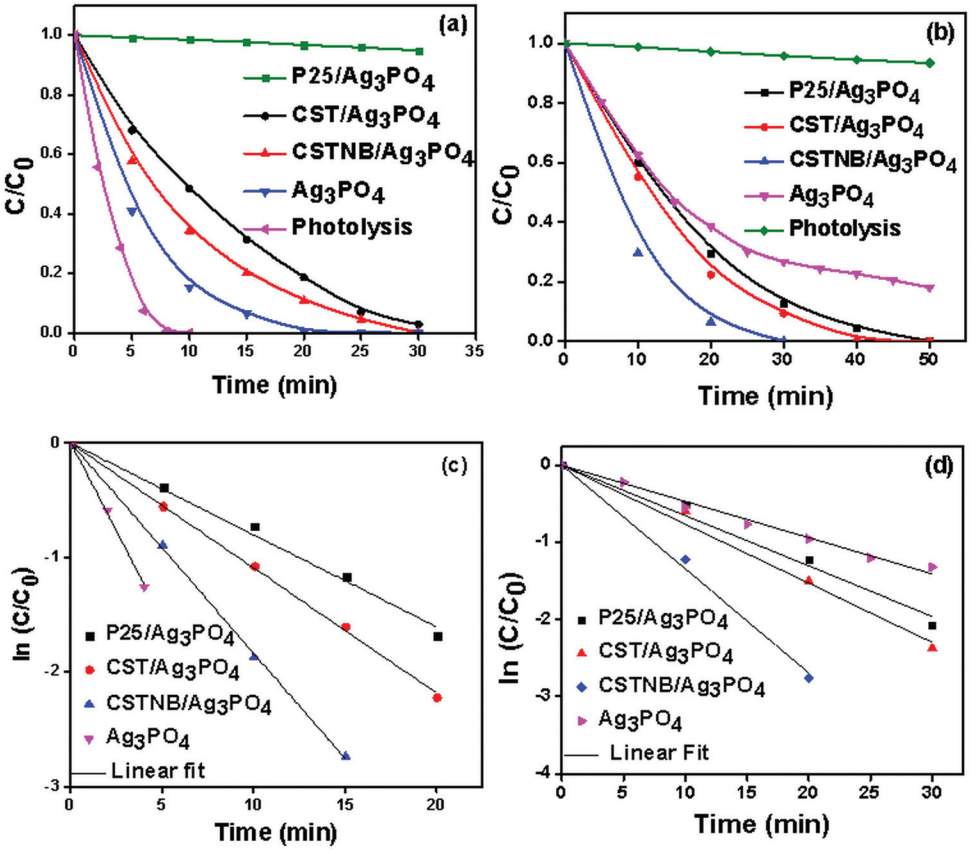

Fig. 6 (a) & (b) Photocatalytic degradation and rate kinetics (c) & (d) of 20 ppm methylene blue and 30 ppm of methyl orange by Ag_3PO_4, Ag_3PO_4/P-25, Ag_3PO_4/CST and Ag_3PO_4/CSTNB under solar irradiation.

Table 1 Rate parameters for photodegradation of methylene blue and methyl orange by Ag_3PO_4, Ag_3PO_4/P-25, Ag_3PO_4/CST and Ag_3PO_4/CSTNB under solar irradiation

	Rate constant, k ($\times 10^{-4}$ min^{-1})	
Catalyst	Methylene blue	Methyl orange
Ag_3PO_4/Degussa P-25	802 ± 2.3	759 ± 87.9
Ag_3PO_4/Combustion synthesized TiO_2	1092 ± 2.1	762 ± 7.2
Ag_3PO_4/Acid etched TiO_2 nanobelts	1840 ± 3.3	1354 ± 6.7
Ag_3PO_4	3096 ± 15.3	445 ± 3.2

carriers take part in the photocatalytic degradation of dyes and bacteria. When Ag_3PO_4 is coupled with TiO_2 nanobelts, the photoactivity is still enhanced by extending the light absorption towards the visible region by the photocatalyst, maintaining stability of the photocatalyst by reducing the release of Ag^+ ions into solution.[45,47,48]

Under dark conditions with Ag_3PO_4 in a bacterial suspension, a bactericidal effect was observed because of the release of Ag^+ ions into the suspension.[47] However, this process occurs at time scales greater than 2 h. Thus the release of Ag does not influence photocatalytic activity for the degradation of dyes but shows some activity towards the inactivation of bacteria. Therefore, it is considered best to employ Ag_3PO_4 as a photocatalyst and investigate the bactericidal effect under UV/solar light. Similarly, using pristine Ag_3PO_4 for methylene blue degradation showed best activity initially but the photoactivity of Ag_3PO_4 decreased over subsequent trials, as discussed in the later section on reusability. This was observed by the decrease in photocatalytic activity and also by observing a change in the color of Ag_3PO_4 from yellow to black because of the formation of Ag nanoparticles upon shining light. But this was not observed when Ag_3PO_4 was impregnated with nanobelt structures, where the latter act as the support preventing decrease in the photoactivity of Ag_3PO_4. Thus Ag_3PO_4 decorated TiO_2 nanobelts are the best for the photocatalytic degradation of dyes and bacteria.

5.7. Scavenger reactions

It is known that the principal factor of photocatalysis is the generation of reactive radicals. Therefore, it is necessary to evaluate the nature of the reactive radicals responsible for the catalytic degradation. The photocatalytic reactant mixture was mixed with various scavengers and the degradation was carried out. EDTA-2Na^+ (hole scavenger),[49] tertiary-butyl alcohol ($^{\bullet}OH$ scavenger),[50] DMSO (e− scavenger),[51] and benzo-

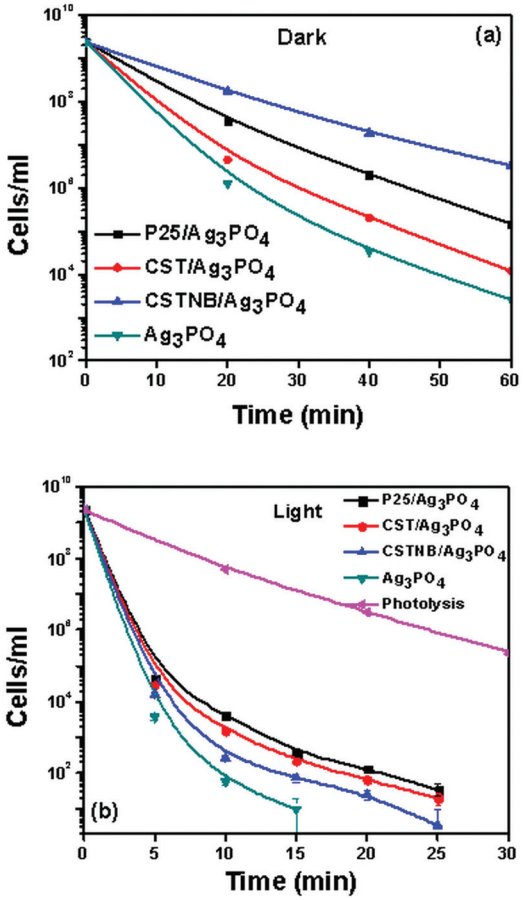

Fig. 7 Antimicrobial activity of Ag_3PO_4, Ag_3PO_4/P-25, Ag_3PO_4/CST and Ag_3PO_4/CSTNB under (a) dark conditions (b) under solar irradiation.

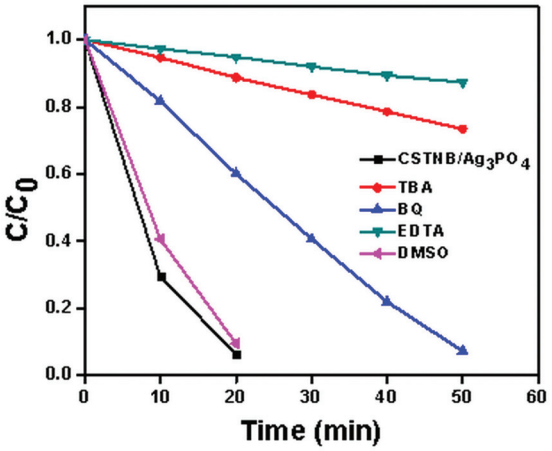

Fig. 8 Evaluation of reactive radical species using various scavengers.

quinone ($O^{\bullet}_2^-$ scavenger)[52] were the scavengers added to the reaction mixture containing methylene blue and catalyst particles and it was subjected to photocatalytic degradation under sunlight. From Fig. 8, it is observed that photocatalytically generated holes and hydroxyl radicals formed during the reaction of Ag_3PO_4 and acid etched TiO_2 nanobelt composites are responsible for the efficient degradation. There is a huge probability for the holes generated from TiO_2 excitation to get transported towards Ag_3PO_4, and thus the generation of hydroxyl radicals is highly favorable. The excited electrons of Ag_3PO_4, in addition to transported electrons from anatase, also take part in the generation of $O^{\bullet}_2^-$ radicals.

5.8. Stability

The reusability of the catalyst has been tested by photo-degrading methylene blue under solar radiation. The catalyst particles were centrifuged and dried at 100 °C after each cycle. The catalytic stability is shown in Fig. 9 as a 3D profile representing methylene blue degradation with respect to each cycle. As compared to the pristine Ag_3PO_4, Ag_3PO_4 impregnated on acid-etched TiO_2 nanobelts shows consistent photocatalytic activity even after 3 cycles. This might be due to the tight

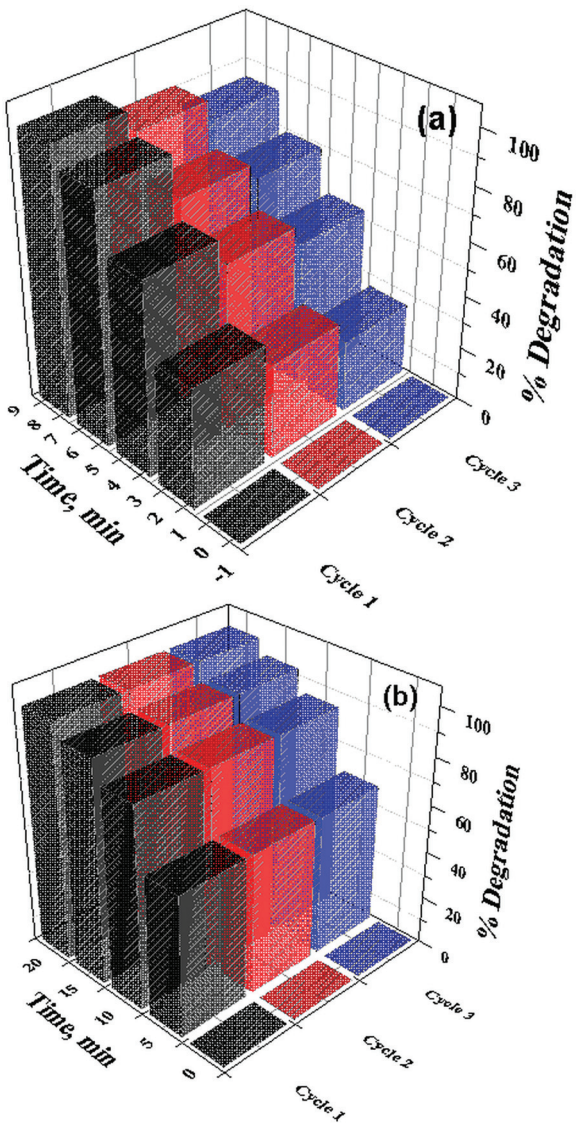

Fig. 9 Reusability of (a)Ag_3PO_4 and (b) Ag_3PO_4/TiO_2 nanobelts against methylene blue degradation.

anchoring of Ag_3PO_4 on the surface of acid etched nanobelts that enhances the stability of the composites.

6. Conclusions

This study indicates the outstanding properties exhibited by the novel combustion synthesis derived TiO_2 nanobelts compared to commercial TiO_2. TiO_2 nanobelts were synthesized using combustion synthesized TiO_2 for the first time. The synthesis and photodegradation experiments of composite Ag_3PO_4 coupled with acid etched combustion synthesized TiO_2 nanobelts were performed. The photocatalytic activity of Ag_3PO_4/CSTNB composites was significantly higher compared to Ag_3PO_4/CST and Ag_3PO_4/P-25. The efficient and excess generation of hydroxyl radicals by the Ag_3PO_4/CSTNB due to lower recombination and better charge transfer led to enhanced photoactivity. TiO_2 islands and Ag_3PO_4 impregnation on top of acid etched TiO_2 nanobelts have not only contributed towards enhanced charge separation but also efficient charge transfer and utilization of a broad spectrum of light for a better photocatalytic activity for the degradation of dyes and inactivation of bacteria.

Acknowledgements

The authors are thankful to the Department of Science and Technology, India for financial support. The authors thank Prof. Jayant Modak, Department of Chemical Engineering, IISc, for extending facilities to perform antibacterial experiments.

References

1 T. Schwartz, W. Kohnen, B. Jansen and U. Obst, Detection of antibiotic-resistant bacteria and their resistance genes in wastewater, surface water, and drinking water biofilms, *FEMS Microbiol. Ecol.*, 2003, **43**, 325–335.
2 D. D. Mara, S. Cairncross and W. H. Organization, *Guidelines for the safe use of wastewater and excreta in agriculture and aquaculture: measures for public health protection/ prepared by Duncan Mara & Sandy Cairncross*, 1989.
3 M. D. Sobsey, Inactivation of health-related microorganisms in water by disinfection processes, *Water Sci. Technol.*, 1989, **21**, 179–195.
4 G. Korotcenkov, The role of morphology and crystallographic structure of metal oxides in response of conductometric-type gas sensors, *Mater. Sci. Eng., R*, 2008, **61**, 1–39.
5 T. M. Shang, J. H. Sun, Q. F. Zhou and M. Y. Guan, Controlled synthesis of various morphologies of nanostructured zinc oxide: flower, nanoplate, and urchin, *Cryst. Res. Technol.*, 2007, **42**, 1002–1006.
6 K. M. Kim, K.-Y. Kang, S. Kim and Y.-G. Lee, Electrochemical properties of TiO_2 nanotube-$Li_4Ti_5O_{12}$ composite anodes for lithium-ion batteries, *Curr. Appl. Phys.*, 2012, **12**, 1199–1206.
7 X. Wu, W. Xing, L. Zhang, S. Zhuo, J. Zhou, G. Wang and S. Qiao, Nickel nanoparticles prepared by hydrazine hydrate reduction and their application in supercapacitor, *Powder Technol.*, 2012, **224**, 162–167.
8 A. Leelavathi, G. Madras and N. Ravishankar, Origin of enhanced photocatalytic activity and photoconduction in high aspect ratio ZnO nanorods, *Phys. Chem. Chem. Phys.*, 2013, **15**, 10795–10802.
9 V. Subramanian, E. Wolf and P. V. Kamat, Semiconductor-metal composite nanostructures. To what extent do metal nanoparticles improve the photocatalytic activity of TiO_2 films?, *J. Phys. Chem. B*, 2001, **105**, 11439–11446.
10 K. Nagaveni, M. Hegde, N. Ravishankar, G. Subbanna and G. Madras, Synthesis and structure of nanocrystalline TiO_2 with lower band gap showing high photocatalytic activity, *Langmuir*, 2004, **20**, 2900–2907.
11 K. Patil, M. Hegde, T. Rattan and S. Aruna, *Chemistry of nanocrystalline oxide materials-Combustion synthesis, properties and applications*, 2008.
12 Z. Zhang, C.-C. Wang, R. Zakaria and J. Y. Ying, Role of particle size in nanocrystalline TiO_2-based photocatalysts, *J. Phys. Chem. B*, 1998, **102**, 10871–10878.
13 K. Nagaveni, M. Hegde and G. Madras, Structure and Photocatalytic Activity of $Ti_{1-x}M_xO_{2\pm\delta}$ (M = W, V, Ce, Zr, Fe, and Cu) Synthesized by Solution Combustion Method, *J. Phys. Chem. B*, 2004, **108**, 20204–20212.
14 W. Jiang, C. An, J. Liu, S. Wang, L. Zhao, W. Guo and J. Liu, Facile aqueous synthesis of β-AgI nanoplates as efficient visible-light-responsive photocatalyst, *Dalton Trans.*, 2014, **43**, 300–305.
15 M. Ge, N. Zhu, Y. Zhao, J. Li and L. Liu, Sunlight-assisted degradation of dye pollutants in Ag_3PO_4 suspension, *Ind. Eng. Chem. Res.*, 2012, **51**, 5167–5173.
16 Y. Sang, L. Kuai, C. Chen, Z. Fang and B. Geng, Fabrication of a Visible-Light-Driven Plasmonic Photocatalyst of $AgVO_3$@AgBr@Ag Nanobelt Heterostructures, *ACS Appl. Mater. Interfaces*, 2014, **6**, 5061–5068.
17 J. S. Kim, E. Kuk, K. N. Yu, J.-H. Kim, S. J. Park, H. J. Lee, S. H. Kim, Y. K. Park, Y. H. Park and C.-Y. Hwang, Antimicrobial effects of silver nanoparticles, *Nanomedicine*, 2007, **3**, 95–101.
18 Y. Liu, L. Fang, H. Lu, L. Liu, H. Wang and C. Hu, Highly efficient and stable Ag/Ag_3PO_4 plasmonic photocatalyst in visible light, *Catal. Commun.*, 2012, **17**, 200–204.
19 H. Zhao, L. Zhang, X. Gu, S. Li, B. Li, H. Wang, J. Yang and J. Liu, Fe_2O_3–AgBr nonwoven cloth with hierarchical nanostructures as efficient and easily recyclable macroscale photocatalysts, *RSC Adv.*, 2015, **5**, 10951–10959.
20 H. Yu, L. Xu, P. Wang, X. Wang and J. Yu, Enhanced photoinduced stability and photocatalytic activity of AgBr photocatalyst by surface modification of Fe(III) cocatalyst, *Appl. Catal., B*, 2014, **144**, 75–82.
21 X. Yang, J. Qin, Y. Jiang, K. Chen, X. Yan, D. Zhang, R. Li and H. Tang, Fabrication of P25/Ag_3PO_4/graphene oxide

heterostructures for enhanced solar photocatalytic degradation of organic pollutants and bacteria, *Appl. Catal., B*, 2015, **166**, 231–240.

22 J.-W. Xu, Z.-D. Gao, K. Han, Y. Liu and Y.-Y. Song, Synthesis of Magnetically Separable $Ag_3PO_4/TiO_2/Fe_3O_4$ Heterostructure with Enhanced Photocatalytic Performance under Visible Light for Photoinactivation of Bacteria, *ACS Appl. Mater. Interfaces*, 2014, **6**, 15122–15131.

23 X. Yang, H. Cui, Y. Li, J. Qin, R. Zhang and H. Tang, Fabrication of Ag_3PO_4-Graphene composites with highly efficient and stable visible light photocatalytic performance, *ACS Catal.*, 2013, **3**, 363–369.

24 H. Cui, X. Yang, Q. Gao, H. Liu, Y. Li, H. Tang, R. Zhang, J. Qin and X. Yan, Facile synthesis of graphene oxide-enwrapped Ag_3PO_4 composites with highly efficient visible light photocatalytic performance, *Mater. Lett.*, 2013, **93**, 28–31.

25 V. Bellat, R. Chassagnon, O. Heintz, L. Saviot, D. Vandroux and N. Millot, A multi-step mechanism and integrity of titanate nanoribbons, *Dalton Trans.*, 2015, **44**, 1150–1160.

26 N. Wu, J. Wang, D. N. Tafen, H. Wang, J.-G. Zheng, J. P. Lewis, X. Liu, S. S. Leonard and A. Manivannan, Shape-enhanced photocatalytic activity of single-crystalline anatase TiO_2 (101) nanobelts, *J. Am. Chem. Soc.*, 2010, **132**, 6679–6685.

27 Z.-Y. Yuan, J.-F. Colomer and B.-L. Su, Titanium oxide nanoribbons, *Chem. Phys. Lett.*, 2002, **363**, 362–366.

28 Y. Wang, G. Du, H. Liu, D. Liu, S. Qin, N. Wang, C. Hu, X. Tao, J. Jiao and J. Wang, Nanostructured Sheets of Ti-O Nanobelts for Gas Sensing and Antibacterial Applications, *Adv. Funct. Mater.*, 2008, **18**, 1131–1137.

29 R. Hernandez-Delgadillo, D. Velasco-Arias, D. Diaz, K. Arevalo-Niño, M. Garza-Enriquez, M. A. De la Garza-Ramos and C. Cabral-Romero, Zerovalent bismuth nanoparticles inhibit Streptococcus mutans growth and formation of biofilm, *Int. J. Nanomed.*, 2012, **7**, 2109.

30 R. Hernandez-Delgadillo, D. Velasco-Arias, J. J. Martinez-Sanmiguel, D. Diaz, I. Zumeta-Dube, K. Arevalo-Niño and C. Cabral-Romero, Bismuth oxide aqueous colloidal nanoparticles inhibit Candida albicans growth and biofilm formation, *Int. J. Nanomed.*, 2013, **8**, 1645.

31 A. D. Mani, P. M. K. Reddy, M. Srinivaas, P. Ghosal, N. Xanthopoulos and C. Subrahmanyam, Facile synthesis of efficient visible active C-doped TiO_2 nanomaterials with high surface area for the simultaneous removal of phenol and Cr (VI), *Mater. Res. Bull.*, 2015, **61**, 391–399.

32 F. M. Hossain, L. Sheppard, J. Nowotny and G. E. Murch, Optical properties of anatase and rutile titanium dioxide: *Ab initio* calculations for pure and anion-doped material, *J. Phys. Chem. Solids*, 2008, **69**, 1820–1828.

33 S. B. Rawal, S. D. Sung and W. I. Lee, Novel Ag_3PO_4/TiO_2 composites for efficient decomposition of gaseous 2-propanol under visible-light irradiation, *Catal. Commun.*, 2012, **17**, 131–135.

34 R. Liu, P. Hu and S. Chen, Photocatalytic activity of Ag_3PO_4 nanoparticle/TiO_2 nanobelt heterostructures, *Appl. Surf. Sci.*, 2012, **258**, 9805–9809.

35 W. Zhou, G. Du, P. Hu, G. Li, D. Wang, H. Liu, J. Wang, R. I. Boughton, D. Liu and H. Jiang, Nanoheterostructures on TiO_2 nanobelts achieved by acid hydrothermal method with enhanced photocatalytic and gas sensitive performance, *J. Mater. Chem.*, 2011, **21**, 7937–7945.

36 W. Teng, X. Li, Q. Zhao, J. Zhao and D. Zhang, In situ capture of active species and oxidation mechanism of RhB and MB dyes over sunlight-driven Ag/Ag3PO4 plasmonic nanocatalyst, *Appl. Catal., B*, 2012, **125**, 538–545.

37 Y. Lei, L.-D. Zhang, G.-W. Meng, G.-H. Li, X. Zhang, C. Liang, W. Chen and S. Wang, Preparation and photoluminescence of highly ordered TiO_2 nanowire arrays, *Appl. Phys. Lett.*, 2001, **78**, 1125–1127.

38 J. Liu, X. Fu, S. Chen and Y. Zhu, Electronic structure and optical properties of Ag_3PO_4 photocatalyst calculated by hybrid density functional method, *Appl. Phys. Lett.*, 2011, **99**, 191903.

39 X. Ma, B. Lu, D. Li, R. Shi, C. Pan and Y. Zhu, Origin of photocatalytic activation of silver orthophosphate from first-principles, *J. Phys. Chem. C*, 2011, **115**, 4680–4687.

40 B. Xin, L. Jing, Z. Ren, B. Wang and H. Fu, Effects of simultaneously doped and deposited Ag on the photocatalytic activity and surface states of TiO_2, *J. Phys. Chem. C*, 2005, **109**, 2805–2809.

41 J. Kiwi and V. Nadtochenko, Evidence for the mechanism of photocatalytic degradation of the bacterial wall membrane at the TiO_2 interface by ATR-FTIR and laser kinetic spectroscopy, *Langmuir*, 2005, **21**, 4631–4641.

42 S. Sontakke, C. Mohan, J. Modak and G. Madras, Visible light photocatalytic inactivation of Escherichia coli with combustion synthesized TiO_2, *Chem. Eng. J.*, 2012, **189**, 101–107.

43 G. Gogniat and S. Dukan, TiO2 photocatalysis causes DNA damage via Fenton reaction-generated hydroxyl radicals during the recovery period, *Appl. Environ. Microbiol.*, 2007, **73**, 7740–7743.

44 Q. Li, S. Mahendra, D. Y. Lyon, L. Brunet, M. V. Liga, D. Li and P. J. Alvarez, Antimicrobial nanomaterials for water disinfection and microbial control: potential applications and implications, *Water Res.*, 2008, **42**, 4591–4602.

45 G. A. Sotiriou and S. E. Pratsinis, Antibacterial activity of nanosilver ions and particles, *Environ. Sci. Technol.*, 2010, **44**, 5649–5654.

46 M. Rai, A. Yadav and A. Gade, Silver nanoparticles as a new generation of antimicrobials, *Biotechnol. Adv.*, 2009, **27**, 76–83.

47 A. Wu, C. Tian, W. Chang, Y. Hong, Q. Zhang, Y. Qu and H. Fu, Morphology-controlled synthesis of Ag_3PO_4 nano/microcrystals and their antibacterial properties, *Mater. Res. Bull.*, 2013, **48**, 3043–3048.

48 X. Yang, J. Qin, Y. Jiang, R. Li, Y. Li and H. Tang, Bifunctional TiO_2/Ag_3PO_4/graphene composites with superior visible light photocatalytic performance and synergistic inactivation of bacteria, *RSC Adv.*, 2014, **4**, 18627–18636.

49 R. Sapkal, S. Shinde, T. Waghmode, S. Govindwar, K. Rajpure and C. Bhosale, Photo-corrosion inhibition and

photoactivity enhancement with tailored zinc oxide thin films, *J. Photochem. Photobiol., B*, 2012, **110**, 15–21.

50 S. Yan, Z. Li and Z. Zou, Photodegradation of rhodamine B and methyl orange over boron-doped g-C_3N_4 under visible light irradiation, *Langmuir*, 2010, **26**, 3894–3901.

51 D. Wang, Y. Duan, Q. Luo, X. Li, J. An, L. Bao and L. Shi, Novel preparation method for a new visible light photocatalyst: mesoporous TiO_2 supported Ag/AgBr, *J. Mater. Chem.*, 2012, **22**, 4847–4854.

52 W. Li, D. Li, S. Meng, W. Chen, X. Fu and Y. Shao, Novel Approach To Enhance Photosensitized Degradation of Rhodamine B under Visible Light Irradiation by the $Zn_xCd_{1-x}S/TiO_2$ Nanocomposites, *Environ. Sci. Technol.*, 2011, **45**, 2987–2993.